

Scientific Report and Bibliography
of the Group of G. Weigelt

1997 — 1999

Young stellar objects, evolved stars, active galactic nuclei, infrared interferometry, and theoretical studies

High-resolution interferometric observations at infrared wavelengths are a powerful tool to investigate the physics of stellar and extragalactic objects. In particular, deeply embedded young stellar objects with disks and outflows, dust-enshrouded stars in late stages of stellar evolution, and active galactic nuclei with dusty tori can be studied. Sufficient angular resolution often cannot be reached by conventional ground-based observations due to the presence of atmospheric turbulence and by HST observations due to the rather small mirror diameter. By means of our bispectrum speckle interferometry method, it is possible to overcome this resolution limitation. Therefore we are able to obtain images which are even sharper than those from the Hubble Space Telescope. For instance, using the Russian SAO 6 m telescope we have for the first time obtained diffraction-limited *K*-band ($2.2 \mu\text{m}$) images with 76 mas resolution and *H*-band ($1.65 \mu\text{m}$) images with 57 mas resolution. The 8-10 m class telescopes, which are now becoming available, will allow us to achieve even higher resolution.

In a few years infrared long-baseline interferometry will revolutionize infrared astronomy as radio interferometry revolutionized radioastronomy during the last decades. It will give complementary information with even higher resolution and thus provides fundamental constraints for theoretical models. We are heavily involved in several interferometry projects, such as the 23 m-baseline Large Binocular Telescope (LBT) and the ESO Very Large Telescope Interferometer (VLTI). We have started to develop instrumentation for the VLTI within the international VLTI AMBER Camera consortium. In collaboration with the interferometry group of the OCA observatory in France, we have built an infrared beam combination instrument which has, for the first time, allowed us to record spectrally dispersed infrared long-baseline interferograms.

In addition to focusing on bispectrum speckle interferometry and long-baseline interferometry, we perform extensive theoretical studies. On the one hand, radiative transfer calculations provide the physical parameters of circumstellar shells, yielding spectral energy distributions and visibility functions for direct comparison with the observations. On the other hand, extensive stellar evolution calculations are carried out, giving detailed information on structure and evolution of the objects. Both observational and theoretical efforts – and in particular their combination – contribute considerably to reveal physical parameters. In other words, our strategy is to combine high-resolution bispectrum speckle interferometry and long-baseline interferometry with the theoretical efforts described above, aiming at a quantitative interpretation of our observations.

The cosmic ray group focuses on the origin of the highest energy cosmic rays and the physics of active galactic nuclei. The aim is to explain the origin, transport and physics

of energetic particles, and their effect in environments ranging from stars to cosmological structure. This work is expanding into high energy particle physics.

1 Young stellar objects

During the earliest stages of their evolution, young stellar objects are embedded in dense dusty circumstellar material. Conventional imaging allows resolving only the outermost parts of the circumstellar environment even in the nearest star forming regions. High spatial resolution thus is a key factor towards an improved understanding of the structure of the circumstellar material, the origin and dynamics of jets and outflows, and the multiplicity of young stellar objects. The resolution we achieve with our bispectrum speckle interferometry enables us to see details as small as 5 to 10 AU in nearby star forming regions and thus allows us to study those regions that may be precursors of planetary systems.

1.1 Young binary stars

It is well known that single stars are a minority. Most stars in our galaxy are found in binary or higher order multiple systems. Thus, multiplicity is a major issue in stellar astrophysics and the formation of binary stars must be an integral part of any theory of star formation. We hope to learn more about the star formation process by investigating the binary statistics of young stars. Another fundamental role of binary studies is to allow direct determination of stellar masses.

Our bispectrum speckle interferometry method is the leading method for obtaining diffraction-limited images of binary stars. One of the projects we have started is a speckle interferometric survey for binaries among the massive stars in the very young Orion Nebula cluster. Using the 6 m SAO telescope, we obtained diffraction-limited images of the four brightest stars in the Orion Trapezium (see Fig. 1) with an unprecedented resolution λ/D of 57 mas and 76 mas in the near-infrared H - and K -band, respectively. The H and K images and visibility functions of Θ^1 Ori C – the star responsible for the proplyds – show for the first time that Θ^1 Ori C is a close binary with a separation of only ~ 33 mas. We have used the magnitudes and colors of the companions to estimate their stellar masses by comparison with evolutionary tracks in the Hertzsprung-Russel diagram.

Additionally, we obtained K' -band ($2.15 \mu\text{m}$) speckle reconstructions of 9 other bright Orion Nebula cluster member stars of spectral type O or B. We found 4 visual companions of these stars. Considering both the visual and the spectroscopic companions of the total sample of 13 target stars, the total number of companions is at least 14. Correcting for the unresolved systems we derived that there are ~ 1.5 companions per primary star on average. This number is clearly higher than the mean number of ~ 0.5 companions per primary star found for the low-mass stars in the Orion Nebula cluster as well as in the field population. This suggests that a different mechanism is at work in the formation of high-mass multiple systems in the dense Orion Nebula cluster than for low-mass stars.

People involved: T. Preibisch, K.-H. Hofmann, D. Schertl, G. Weigelt

Collaborations: Y. Balega, I. Balega (SAO); M. Schöller (ESO); H. Zinnecker (AIP)

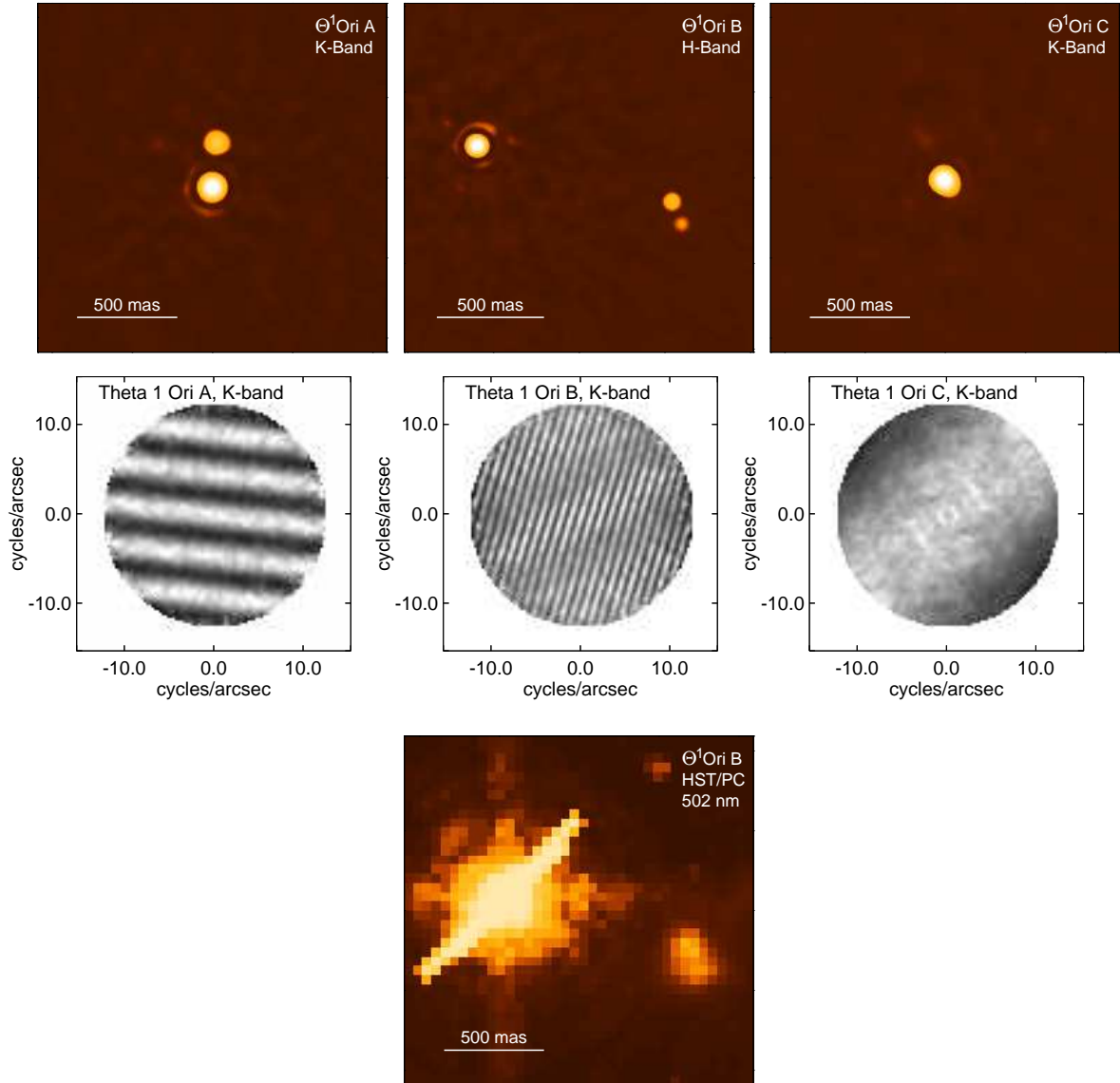


Figure 1: Infrared speckle reconstructions and visibility functions of Θ^1 Ori A, B, and C and, for comparison, the HST optical $0.5 \mu\text{m}$ image of Θ^1 Ori B (WFPC2 camera, i.e. after repair mission; separation of the close binary B_2B_3 on the right hand side is approx. $0''.114$). Since no infrared HST image exists which resolves Θ^1 Ori B_2B_3 , we can only compare our $1.65 \mu\text{m}$ infrared speckle reconstruction with this visual $0.5 \mu\text{m}$ HST image (the diagonal bar-like feature in the HST image is an artefact).

1.2 Embedded young stellar objects with outflows

The young outflow object S140 IRS1. Some – perhaps all – newly formed stars go through a turbulent phase of adolescence in which they eject streams of gas that collide with the surrounding molecular cloud material. Figure 2 shows the first bispectrum speckle interferometry image and the first high-resolution speckle polarimetry observations of the young stellar object S140 IRS1 and its southern outflow. Radio interferometric observations in the HCO^+ $J=1-0$ line proved that this outflow is in fact bipolar. The northern lobe shows redshifted emission and is thus pointing away from us. Consistently, the northern part of the outflow cavity is not visible at near infrared wavelengths. The observations suggest that S140 IRS1 is a massive young star surrounded by an optically thick circumstellar disk. The outflow perpendicular to this disk is clearing a polar cavity which can be seen in scattered stellar light.

The interpretation of our high-resolution observations of young stellar objects with circumstellar material requires detailed modelling and depends crucially on the application of adequate methods of solution of the radiation transfer problem. We use a fully two-dimensional frequency-dependent code to compute a self-consistent solution of the radiation transfer problem within the framework of the flux-limited diffusion approximation. The structure of the circumstellar material is assumed to be axisymmetric, but can otherwise have arbitrary geometry. Thus, we can model density distributions with a wide variety of structures, including disks, envelopes, tori, and cavities. The first part of our code computes the distribution of dust temperatures and mean radiation intensities on a set of nested grids. In a second step a ray-tracing procedure is used to calculate intensity maps at several wavelengths and the spectral distribution of the emitted flux. Very recently, we have started radiation transport simulations to model the speckle interferometric images of S140. Some

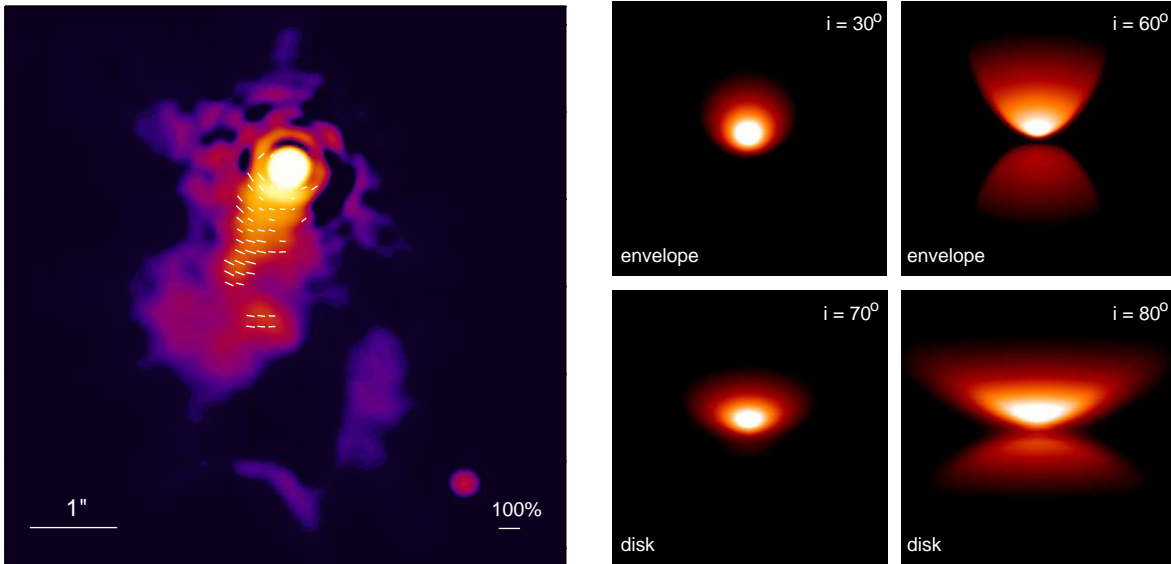


Figure 2: (left) High-resolution bispectrum speckle interferometry and speckle polarimetry of the southern outflow lobe of S140 IRS1. (right) Radiative transfer simulation of a young stellar object (top images) embedded in a spherical dusty envelope with empty parabolic cavities or (bottom images) with a Keplerian disk. We show $2 \mu\text{m}$ images for different inclination angles i .

examples for model images of young stellar objects with envelopes or disks are shown in Fig. 2.

The Becklin-Neugebauer object. The Kleinmann-Low nebula is the site of most recent high-mass star formation in Orion. High-resolution observations at infrared to radio wavelengths have revealed the complex structure of this region. Nevertheless, not much information is available on the structure of the brightest infrared source within this nebula which is known as the Becklin-Neugebauer object (BN).

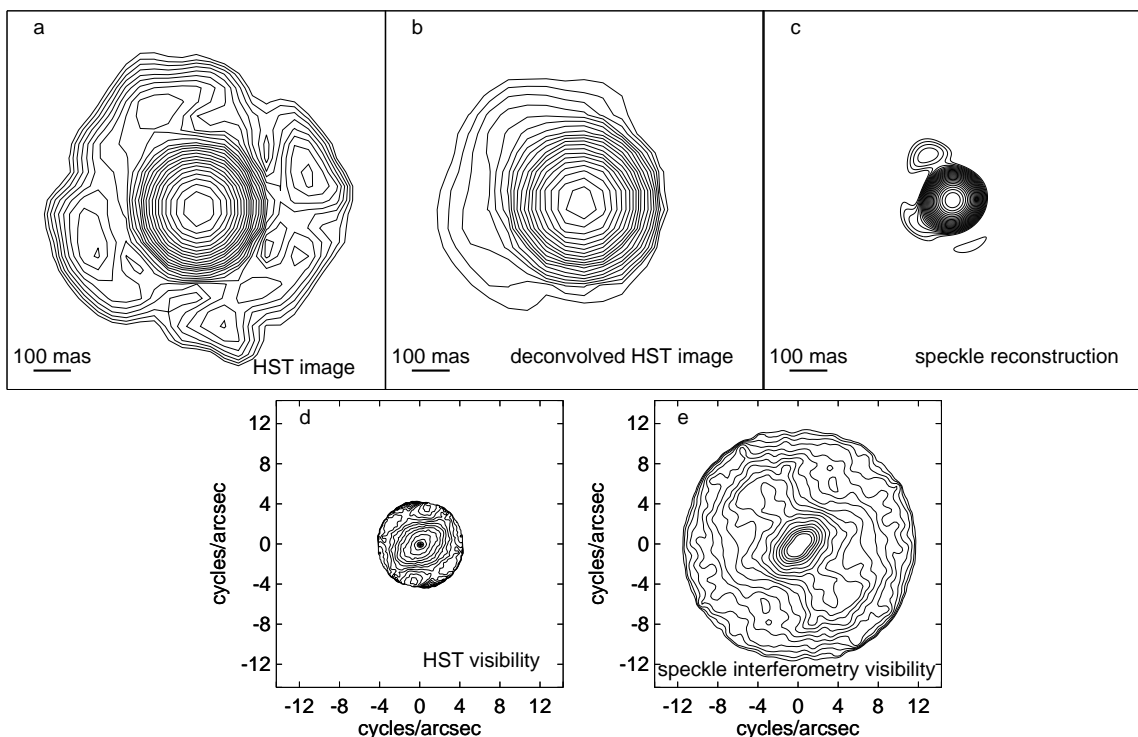


Figure 3: (a) $2 \mu\text{m}$ HST continuum image of BN (archival HST image). Most of the structure is due to the telescope diffraction pattern. (b) Deconvolved $2 \mu\text{m}$ HST image. (c) $2 \mu\text{m}$ bispectrum speckle interferometry image of BN. For illustration of the uv -plane coverage (d) and (e) show the HST and the speckle visibility functions, respectively. In all plots north is up and east to the left.

Our $2 \mu\text{m}$ near-infrared (NIR) observations of BN with the SAO 6 m telescope show the presence of small-scale structures which were previously unknown. Fig. 3 shows images (a,b,c) and visibilities (d,e) of BN and, for comparison, HST archive data. The resolution of our bispectrum speckle interferometry reconstruction (Fig. 3c) is 80 mas. In addition to a larger nebula, an asymmetric dominant southern component and a rather faint component approx. 140 mas to the north-east (position angle 30°) can be identified. The southern component is resolved with a uniform disk diameter of approx. 50 mas (~ 22 AU). BN is known to be the source of an ionized wind with a recombination radius of comparable size. This suggests that the components in our image consist of contributions from attenuated direct light from the unresolved star and from thermal radiation from the optically thick dust environment outside the wind cavity. The asymmetry of the southern component with an elongation towards the southeast (position angle 125°) can thus be understood to be due to an asymmetry of the dust distribution. Our observations are consistent with a bipolar outflow structure and a

position angle of the polar axis of about 30° .

Using the bispectrum speckle interferometry method we have also obtained diffraction-limited 76 mas resolution *K*-band images of the Herbig Ae/Be object LkH α 198. For the interpretation of this image we have carried out 2D radiative transfer calculations of both unpolarized and polarized light. Furthermore, we have started studies of various other young stellar objects, for instance, the jet source DG Tau, the GG Tau circumbinary disk, the Taurus Class I object IRAS 04302+2247 with its edge-on silhouette disk, and the bipolar outflow source R Mon.

People involved: T. Preibisch, T. Hannemann, K.-H. Hofmann, R. Osterbart, D. Schertl, G. Weigelt.

Collaborations: W. Duschl (Univ. Heidelberg); O. Fischer (Univ. Jena); H. Zinnecker (AIP)

2 Stars in late stages of stellar evolution: AGB stars, post-AGB objects, and massive supergiants

Stars are an important constituent of galaxies and are exclusively responsible for the production, reprocessing and dissemination of heavier elements. The existence of these elements provides the necessary prerequisite to establish chemical reactions under suitable conditions which then ultimately lead to the formation of organic molecules. Hence, it is of considerable importance to acquire a precise knowledge of all the complex physical processes that occur inside the stars, in their envelopes, and also in the flow of matter from their surfaces into the interstellar medium. Particularly, the late stages of stellar evolution play a crucial role for the understanding of the galactic chemodynamical evolution. The erosion of the stellar surfaces by strong winds leads to the chemical enrichment of the interstellar medium being manifested by the formation of circumstellar shells. Our investigation of late evolutionary phases include massive supergiants as well as Asymptotic Giant Branch (AGB) stars and their immediate successors, the nuclei of proto-planetary nebulae.

Mass loss is one of the dominant effects on the evolution of massive stars virtually leading to an almost complete peeling of the star. Circumstellar dust shells found around evolved massive stars (supergiants) often show features of non-spherical outflows. Observing and modelling the circumstellar shells surrounding these stars, unveil details of evolution as, for instance, mass-loss rates. The presence of fossil shells even give clues for the evolutionary history.

The vast majority of all stars in the universe which have left their main sequence phase are, however, of low and intermediate mass and evolve through the AGB phase. These luminous, frequently pulsating and heavily mass-losing AGB stars form an important stellar population which contributes considerably to light, chemistry and dynamics of galaxies. The envelopes of AGB stars are the major factories of cosmic dust. Accordingly, AGB stars are heavily enshrouded by dust exposing high fluxes in the infrared and are ideal laboratories to investigate the interplay between various physical and chemical processes.

2.1 The photospheres of Mira stars

The resolution of bispectrum speckle interferometry observations with the SAO 6 m telescope at $\lambda \sim 700$ nm is 30 mas which is high enough to resolve the stellar disks of nearby Mira

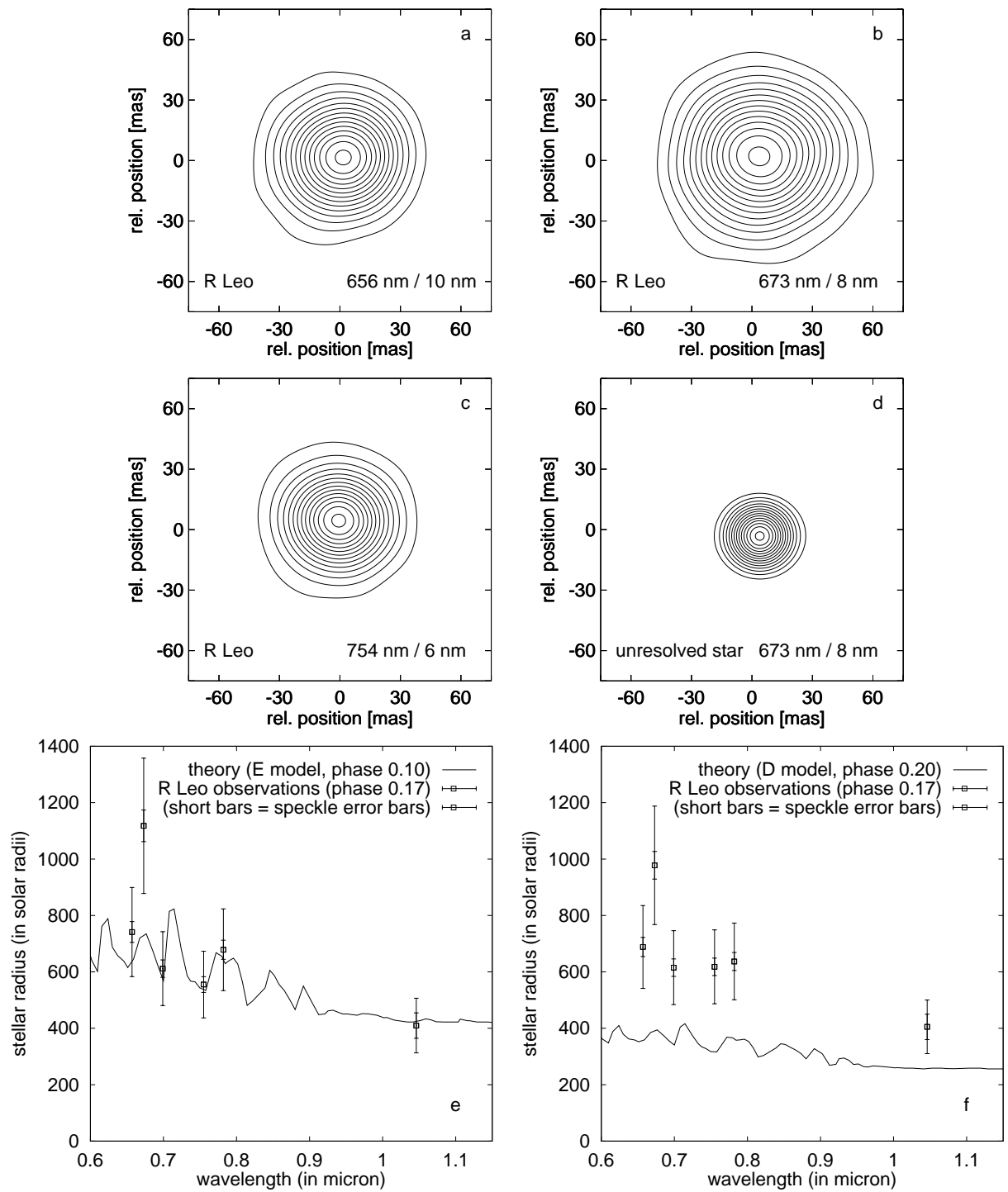


Figure 4: (a-d) Diffraction-limited bispectrum speckle interferometry reconstructions of R Leo and the unresolved star HIC 49637. In each panel the contour levels are plotted from 7-98% of peak intensity in steps of 7%. The uniform disk diameters of R Leo at the wavelengths 656 nm, 673 nm, 699 nm, 754 nm, 781 nm, and 1045 nm were determined to be 61 mas, 76 mas, 53 mas, 49 mas, 55 mas, and 38 mas, respectively. (e,f) Measured and theoretical $\tau_{\lambda}=1$ radii of R Leo (E and D model; $\sim 75\%$ of the errors are caused by the Hipparcos parallax error).

stars, to reveal photospheric asymmetries, and to study the strong wavelength dependence of the diameter and its variability. In strong TiO absorption bands, the diameter of M-type Mira variables is approximately twice as large as in the continuum. Theoretical studies show that observed monochromatic radii are a very sensitive diagnostic tool for investigating the structure of Mira photospheres. We have observed the Mira stars R Cas and R Leo through filters with bandwidths of only 6 nm to 10 nm in the wavelength range from 673 nm to 1045 nm. With these filters, quasi-monochromatic radii were measured in strong TiO absorption bands (at 673 nm and 714 nm), moderate TiO absorption bands (700 nm), and in the continuum (1045 nm). These measurements were suitable for comparison with diameter predictions of Mira star models. Fig. 4 presents diffraction-limited bispectrum speckle interferometry reconstructions of R Leo. The reconstructions show, for example, that the uniform disk diameter of R Leo is $76 \text{ mas} \pm 3 \text{ mas}$ in the strong TiO absorption band at 673 nm and only $38 \text{ mas} \pm 4 \text{ mas}$ in the continuum at 1045 nm. These images together with our R Cas images are the highest resolution optical images to date of a Mira star.

We have compared our observations with theoretical Mira star models of Bessel, Scholz, and Wood (1996). These models differ in pulsation mode, mass, and luminosity. Wavelength-dependent $\tau_\lambda=1$ radii were derived from the observed visibilities by application of model-predicted center-to-limb intensity variations. Adopting the HIPPARCOS parallaxes we obtained linear stellar radii. A photospheric radius (Rosseland radius) of $410 \pm 90 R_\odot$ was derived from the 1045 nm continuum measurement for R Leo. From the 1045 nm radius combined with flux measurements, an effective temperature of $2600 \text{ K} \pm 150 \text{ K}$ was determined. Fig. 4 shows a comparison of the measured linear $\tau_\lambda=1$ radii of R Leo with the theoretical radii. The E model (one of the 5 models presented by Bessel, Scholz and Wood; first overtone mode, $1 M_\odot$, $6310 L_\odot$, $366 R_\odot$, 2700 K) gives the best agreement with our measurements of R Leo (but there are considerable differences at two wavelengths). All other models (e.g. the fundamental mode D model with $1 M_\odot$, $3470 L_\odot$, $236 R_\odot$, 2900 K ; see Fig. 4) are clearly not representative of R Leo. Figure 4 illustrates that comparison of the observed monochromatic $\tau_\lambda=1$ radii with the model radii can provide important information for the modelling of Mira photospheres.

People involved: T. Blöcker, K.-H. Hofmann, G. Weigelt.

Collaborations: Y. Balega (SAO); M. Scholz (Univ. Heidelberg); P. Wood (Mount Stromlo and Siding Spring Obs.)

2.2 The infrared sources AFGL 2290 and CIT 3: Opaque dust shells around oxygen-rich AGB stars

The extreme mass loss of AGB stars substantially affects the appearance of these objects. We have chosen CIT 3 (IRC +10 011) and AFGL 2290 (OH 39.7+1.5) for our studies of oxygen-rich AGB stars because they are typical examples of moderately to highly obscured variable OH/IR stars with corresponding high mass-loss rates.

Our bispectrum speckle interferometry observations with the SAO 6 m telescope provided the first diffraction-limited images of the dust shells of oxygen-rich AGB stars. For instance, a 75 mas resolution image of AFGL 2290 was reconstructed for the wavelength $2.11 \mu\text{m}$ (Fig. 5). The image reveals that the circumstellar dust shell of AFGL 2290 is non-spherical. The visibility function shows that the stellar contribution to the total $2.11 \mu\text{m}$ flux is less than $\sim 40\%$. The FWHM Gauss fit diameter of AFGL 2290 at $2.11 \mu\text{m}$ is $35 \text{ mas} \times 40 \text{ mas}$

which corresponds to a diameter of $34 \text{ AU} \times 39 \text{ AU}$ for an adopted distance of 0.98 kpc .

These new high spatial resolution measurements provided strong constraints for our extensive radiative transfer calculations for the dust shell of AFGL 2290 supplementing the information provided by the spectral energy distribution. Both the visibility and the spectral energy distribution can be well reproduced by a model with a larger grain radius and a higher optical depth than indicated by the observed spectral energy distribution (SED) alone. Our radiative transfer model demonstrates the possible limitations of dust shell models which are constrained solely by the spectral energy distribution and emphasizes the importance of high spatial resolution observations for the determination of the structure and the properties of circumstellar dust shells around evolved stars.

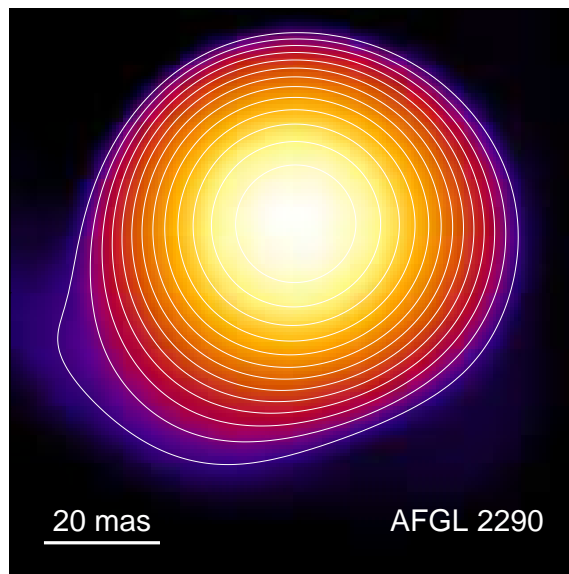


Figure 5: 75 mas bispectrum speckle interferometry of AFGL 2290. The contour level intervals are 0.25 mag . The lowest contour level is 3.25 mag fainter than the peak intensity.

People involved: T. Blöcker, A. Gauger, K.-H. Hofmann, R. Osterbart, G. Schniggenberg, G. Weigelt.

Collaborations: Y. Balega (SAO)

2.3 Temporal evolution and mass loss of extreme carbon stars

IRC +10 216. The AGB star IRC +10 216 (CW Leo) is the nearest and best-studied carbon star and one of the brightest infrared sources. It experiences a strong mass loss with a rate of $\dot{M} \approx 2 - 5 \cdot 10^{-5} M_{\odot}/\text{yr}$. The central star of IRC +10 216 is a long-period variable star (LPV) with a period of approx. 649 days. Recent estimates for its distance range from 110 pc to 150 pc .

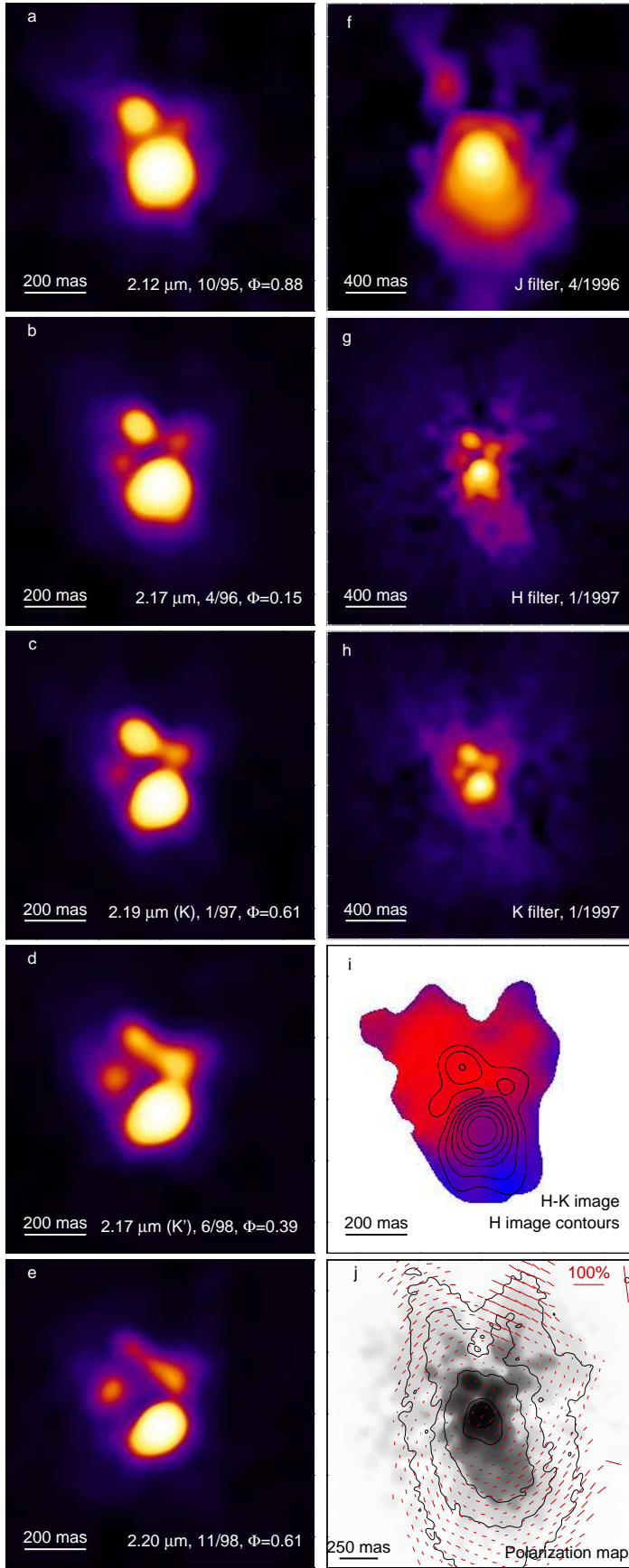


Figure 6: High-resolution bispectrum speckle interferometry images of IRC +10 216. North is up and east to the left.

The figures (a) to (e) represent a time series showing the evolution of the subarcsecond structure of IRC +10 216 from 1995 (top) to 1998 (bottom). In these figures the same color level corresponds to the same relative intensity measured with respect to the peak. In all figures the center wavelength of the filter and the photometric phase Φ are indicated.

Figures (f) to (h) show the wavelength dependence of the structure of IRC +10 216 ((f) *J*-band 149 mas resolution, (g) *H*-band 70 mas resolution, and (h) *K*-band 87 mas resolution). (i) *H* – *K* color image of the central region of IRC +10 216. Red corresponds to $H - K = 4.6$ and blue to $H - K = 2.1$. The color at the position of the brightest component (A) is $H - K = 3.2$. The contours are those of the *H*-band image with a spacing of 0.5 mag. (j) Superposition of the total intensity at 1.1 μm (contours are at $5^{\text{m}}0$, $4^{\text{m}}2$, $3^{\text{m}}4$, $1^{\text{m}}8$, and $1^{\text{m}}0$ relative to the peak) derived from the archival HST polarization data and the negative *H* speckle image. The polarization vectors are shown in red.

We have reconstructed high-resolution J -, H -, and K -band images and the first $H - K$ color image of IRC +10 216 (Fig. 6). The images were derived from 6 m telescope speckle interferograms using the bispectrum speckle interferometry method. At each of our five epochs, observations were made at wavelengths within the K -band ($2.0 - 2.4 \mu\text{m}$, Figs. 6a to e and h). These observations are the highest resolution infrared study to date of a carbon star. Figure 6j shows $1.1 \mu\text{m}$ HST polarimetry (photometric phase $\Phi = 0.76$; raw data retrieved from the Hubble Data Archive, STScI). Total intensity, degree and position angle of the polarization were derived from these data.

The H and K images consist of several compact components within a $0''.2$ radius and a fainter asymmetric nebula. For the first time, our images show – almost like a movie of five frames – the dynamical evolution of the inner nebula. We denote the brightest components in the 1996 image as A, B, C, and D in the order of decreasing brightness. For instance, the separation of the two brightest components A and B increased by almost 40% from 191 mas in 1995 to 265 mas in 1998 corresponding to a tangential velocity of $\sim 23 \text{ mas/yr} \sim 14 \text{ km/s}$ (for a distance of 130 pc). At the same time, component B is fading and the components C and D become brighter. Our high-resolution $H - K$ color image (Fig. 6i) shows that the components B, C, and D are very red in comparison with the integral color. The brightest component A as well as the *cometary southern tails* in the H and J images are comparatively blue. This suggests that component A is produced to a significant fraction by scattering of stellar light and, furthermore, that the dust shell is not spherically symmetric. The polar axis probably points towards us with its southern side (southern cometary lobe A).

The polarization pattern (Fig. 6j) is predominantly centro-symmetric. The fact that the center of the polarization pattern does not coincide with A, but is located significantly north of the cometary lobe A, suggests that A is not the star but a southern outflow lobe. The interpretation of A as a scattering lobe is in agreement with our two-dimensional radiative transfer calculations which show that the central star is actually at or near B, between the northern and southern J -band lobes separated by $\sim 500 \text{ mas}$. The polar axis is inclined by approx. 50° with respect to the plane of the sky. If the star is located at or near B, the components A, C, and D and the two J -band lobes are located close to the inner boundary of the dust shell at separations of $\sim 200 \text{ mas} \sim 26 \text{ AU}$ (projected distance) ~ 6 stellar radii for a distance of $\sim 130 \text{ pc}$. The observed changes are consistent with the assumption of an enhanced mass loss since 1997.

The X-shaped bipolar structure of the nebula, most prominently present in the J -band image, most likely implies an asymmetric mass loss. Such asymmetries are often present in protoplanetary nebulae but are unexpected for AGB stars. IRC +10 216 is thus likely to be very advanced in its AGB evolution. It is even possible that it has entered the phase of transformation into a protoplanetary nebula.

CIT 6. The AGB star CIT 6 is an extreme carbon star which is very similar to IRC +10 216. Its infrared colors suggest that it is heavily obscured and that it experiences a strong mass loss. Our bispectrum speckle interferometry observations confirm indirect evidence for an asymmetric structure of the dust shell. A fit to the visibility ($\lambda = 2.17 \mu\text{m}$) yields an estimate for the extent (FWHM of a Gaussian) of the inner part of the dust shell of $46 \text{ mas} \times 36 \text{ mas}$ ($18 \text{ AU} \times 14 \text{ AU}$).

People involved: T. Blöcker, K.-H. Hofmann, A. Men'shchikov, R. Osterbart, G. Weigelt.

Collaborations: A.J. Fleischer, J.M. Winters (Univ. Berlin)

2.4 From the AGB to protoplanetary nebulae

Red Rectangle. The Red Rectangle (AFGL 915) is a famous reflection nebula around the spectroscopic binary HD 44179 at a distance of ~ 330 pc. One of the two stars is a post-AGB star. The separation of the two stars is ~ 0.5 AU which is much smaller than the typical size of an AGB star. This and the peculiar chemical abundances in the stellar atmosphere lead to the conclusion that HD 44179 has undergone a common envelope phase.

Figs. 7 a to c show the first diffraction-limited K -band image of the Red Rectangle with 76 mas resolution, an H -band image with 75 mas resolution, and an RG 715 filter image (~ 800 nm wavelength) with 78 mas resolution (corresponding to 25 AU for a distance of 330 pc). The H and K images were reconstructed from 6 m telescope speckle data and the RG 715 image from ESO 2.2 m telescope data using the bispectrum speckle interferometry method. At all wavelengths the images show a compact, highly symmetric bipolar nebula, suggesting a toroidal density distribution of the circumstellar material. No direct light from the central binary can be seen as it is obscured by a dust disk or circumbinary torus. Our first high-resolution $H - K$ color image of the nebula shows a broad red plateau of $H - K \approx 2$ in the bright inner regions.

The optical and near-infrared images and the available photometric continuum observations in a wide range of ultraviolet to centimeter wavelengths enabled us to model the Red Rectangle in detail using a *two-dimensional* radiative transfer code. Our derived model matches both the high-resolution images and the spectral energy distribution (see Fig. 7h) of this object very well, making the following picture much more certain: The central close binary system is embedded in a very dense, compact circumbinary torus. The dense inner region of this torus extends from an inner radius of $R \approx 6$ AU to an outer radius of $R \approx 30$ AU (91 mas) and has a $\rho \propto r^{-2}$ density distribution. The full opening angle of the bipolar outflow cavities in our model is 70° . By comparing the observed and theoretical images, we derived an inclination angle of the torus to the line of sight of 7° . The radiative transfer calculations also show that the dust properties in the Red Rectangle are spatially inhomogeneous. The modelling confirms that the idea of large grains in the long-lived disk around the Red Rectangle (Jura et al. 1997) is quantitatively consistent with the observations.

People involved: T. Blöcker, A. Men'shchikov, R. Osterbart, G. Weigelt.

Collaborations: Y. Balega (SAO)

2.5 Massive supergiants

Within a systematic investigation of the evolution and morphology of circumstellar dust shells of massive stars, bispectrum speckle interferometry observations were carried out for several prominent supergiants, viz. IRC +10 420, ρ Cas, μ Cep, NML Cyg, and VY CMa. The speckle interferograms were obtained with the SAO 6 m telescope (IRC +10 420, ρ Cas, μ Cep, NML Cyg) and the ESO 3.6 m telescope at La Silla (VY CMa).

The non-spherical dust shell of VY CMa. The red supergiant VY CMa is a key target for the study of massive star evolution. Optical and NIR images at wavelengths $\sim 0.8 \mu\text{m}$, $1.28 \mu\text{m}$, and $2.17 \mu\text{m}$ were reconstructed from 3.6 m telescope speckle data (see Fig. 8). All images clearly show that the circumstellar envelope of VY CMa is non-spherical. The $0.8 \mu\text{m}$, $1.28 \mu\text{m}$, and $2.17 \mu\text{m}$ FWHM Gauß fit diameters are $67 \text{ mas} \times 83 \text{ mas}$, $80 \text{ mas} \times 116 \text{ mas}$ and 138

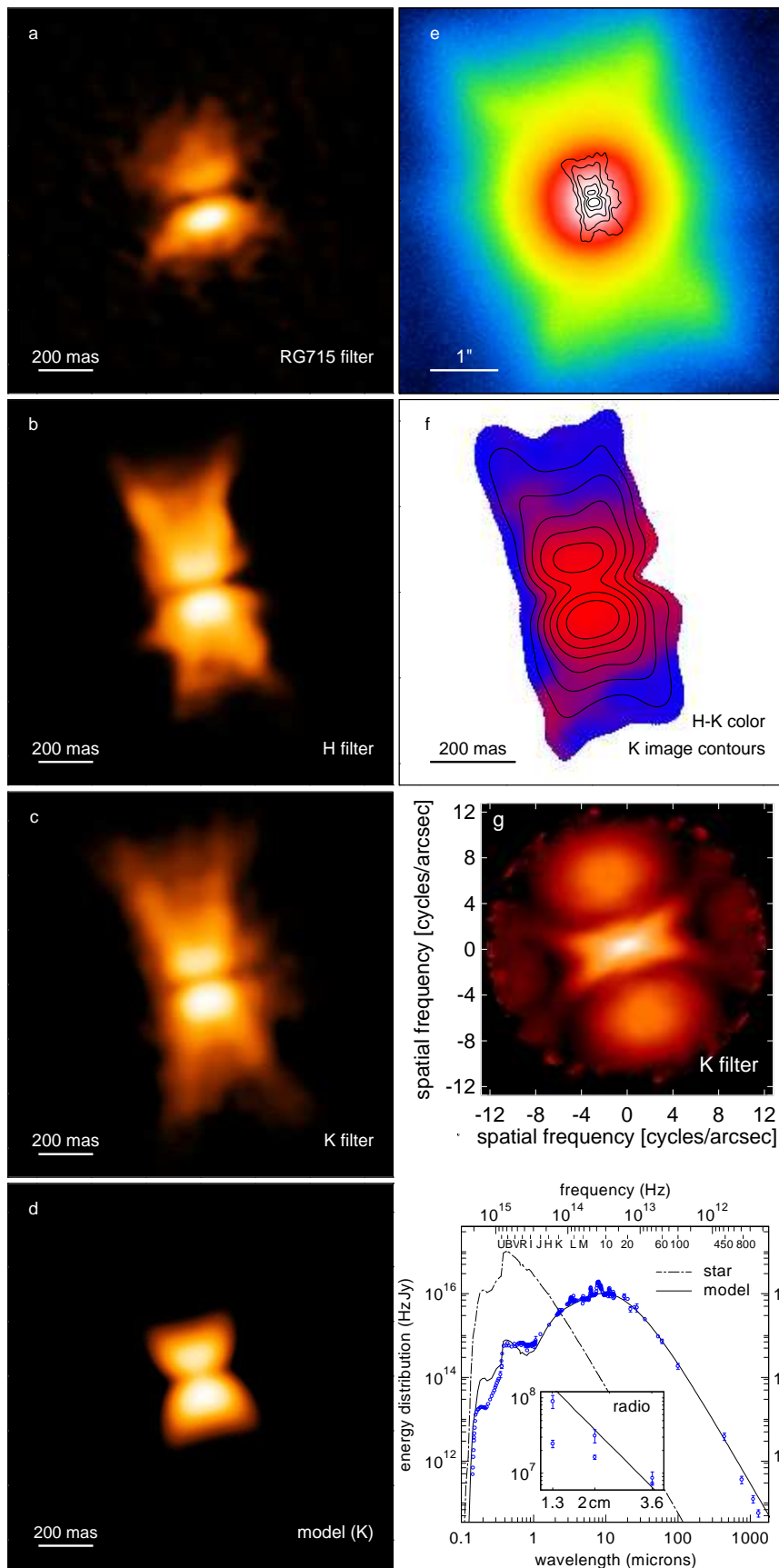


Figure 7: Bispectrum speckle interferometry of the Red Rectangle: (a) RG715 filter; (b) H filter; (c) K filter; (d) Radiative transfer model image for the K-band; (e) Overlay of the RG715 long-exposure and the high-resolution K image; (f) H-K image, red corresponds to $H-K \approx 2.0$ and blue to $H-K \approx 1.2$; (g) Two-dimensional K-band visibility; (h) Observed (blue symbols) and radiative transfer model SED (solid line)

mas \times 205 mas, respectively, or 100AU \times 125AU, 120AU \times 174AU and 207AU \times 308AU ($d = 1.5$ kpc). Possible interpretations of the asymmetric morphology are a circumstellar envelope consisting of an obscuring disk and a bipolar outflow, a stochastic mass loss mechanism as recently detected in IRC +10 216 or a disk-like envelope. Combining recent results about the angular momentum evolution of red supergiants and their pulsational properties, it can be concluded that VY CMa is in the final stage of its evolution along the supergiant branch.

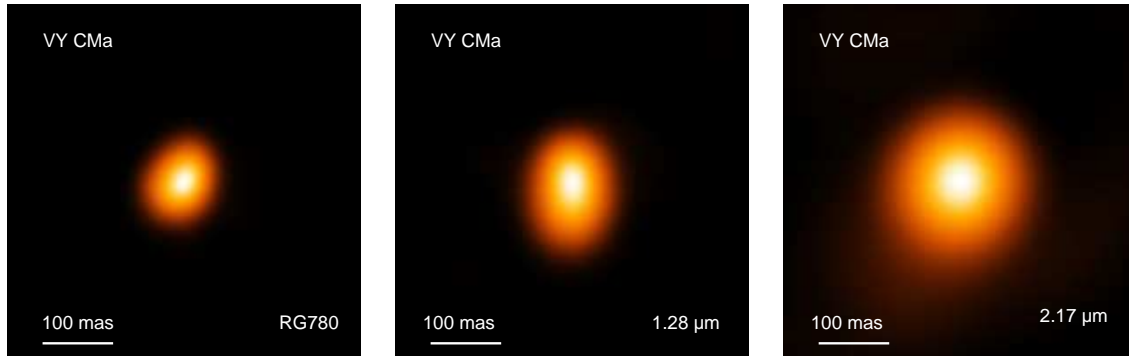


Figure 8: Diffraction-limited 0.8 μm (left), 1.28 μm (middle) and 2.17 μm (right) bispectrum speckle interferometry images of VY CMa. North is at the top and east to the left.

The red supergiant NML Cyg. The star NML Cyg is an extremely red object due to strong obscuration by circumstellar dust. It is a highly evolved OH/IR supergiant of very large luminosity (spectral type M6 I) which suffers from large mass-loss ($\sim 1.5 \cdot 10^{-4} M_{\odot}/\text{yr}$). It is supposed to be among the most luminous supergiants ($\sim 5 \cdot 10^5 L_{\odot}$) in the Galaxy. We obtained diffraction-limited 2.13 μm images with 73 mas resolution at the 6 m telescope and clearly resolved the circumstellar shell of NML Cyg. There is only marginal evidence for deviations from spherical symmetry. The visibility function declines towards the diffraction limit to ~ 0.6 . We performed radiative transfer calculations assuming spherical symmetry to model the spectral energy distribution and visibility functions.

The hypergiant IRC +10 420: Evolution on human timescales. The hypergiant IRC +10 420 is a unique object for the study of stellar evolution since it is the *only object* which is believed to be currently observed in its rapid transition from the red supergiant stage to the Wolf-Rayet phase. Its spectral type changed from F8 in 1973 to mid-A today corresponding to an effective temperature increase of 1000–2000 K within only 25 yr. The massive nature of IRC +10 420 (initially ~ 20 to $40 M_{\odot}$) can be concluded from its distance ($d = 3\text{--}5$ kpc) and large wind velocity (40 km/s) ruling out the alternative post-AGB scenario of a star evolving through the proto-planetary nebula stage.

We have carried out the first speckle observations of IRC +10 420 with 73 mas resolution. Both radiative transfer and stellar evolution calculations were performed for the interpretation of the observations. A diffraction-limited 2.11 μm image of IRC +10 420 was reconstructed from speckle interferograms using bispectrum speckle interferometry. Figure 9 (top left panel) shows the azimuthal average of the reconstructed 2.11 μm visibility function of IRC +10 420 revealing that the central star contributes $\sim 60\%$ and the dust shell $\sim 40\%$ to the total flux. Figure 9 (top right panel) displays the azimuthally averaged diffraction-limited images of IRC +10 420 and the unresolved reference star HIP 95447.

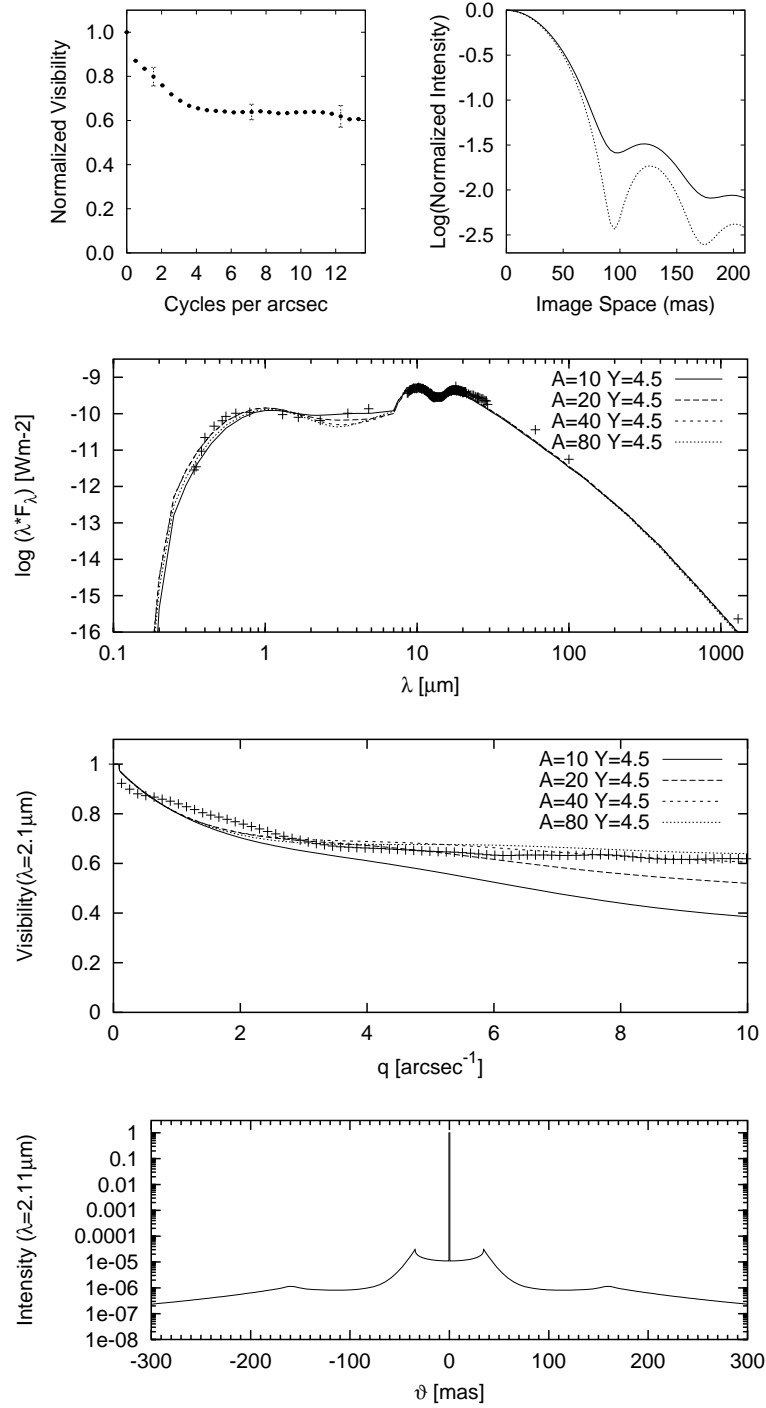


Figure 9: From top to bottom: (1) Azimuthally averaged $2.11 \mu\text{m}$ visibility of IRC +10 420 (left) and azimuthally averaged diffraction-limited $2.11 \mu\text{m}$ images (right) of IRC +10 420 (solid line) and the unresolved reference star HIP 95447 (dashed line). (2,3) SED and visibility for a superwind model with density enhancements of different amplitudes A at $Y = r/r_1 = 4.5$ (r_1 : inner dust-shell radius; +: observations). (4) Model intensity distribution derived from radiative transfer calculations for the above SED and visibility function.

The spectral energy distribution (SED) of IRC +10420 is shown in Fig. 9 as well. In order to model both the spectral energy distribution and the visibility function, we performed radiative transfer calculations assuming spherical symmetry. Since single-shell models fail to reproduce the observed SED, we introduced a two-component shell. For that purpose, we assume that IRC +10420 had passed through a superwind phase in its history as can be expected from its evolutionary status. A previous superwind phase leads to changes in the density distribution, i.e. there is a region in the dusty shell which shows a density enhancement over the normal r^{-2} distribution. The best model for *both* SED *and* visibility was found for a dust shell with a dust temperature of 1000 K at its inner radius of $70R_*$. At a distance of $310R_*$, where the dust temperature has dropped to 480 K, the density is enhanced by a factor of 40. The angular diameters of these components are 69 mas and 311 mas (stellar diameter ~ 1 mas for $d = 5$ kpc). This can be interpreted in terms of an enhanced mass-loss phase roughly 100 years ago. The mass-loss rates of the components can be determined to be $\dot{M}_1 = 7.0 \cdot 10^{-5} M_\odot/\text{yr}$ and $\dot{M}_2 = 1.1 \cdot 10^{-3} M_\odot/\text{yr}$.

People involved: T. Blöcker, J. Lichtenthäler, R. Osterbart, G. Weigelt, M. Wittkowski.

Collaborations: Y. Balega (SAO); N. Langer (Univ. Potsdam); R. Oudmaijer (London)

2.6 Stellar structure and evolution

We perform extensive stellar evolution calculations for various phases of stellar evolution covering all stages from the pre-main sequence regime towards the domain of white dwarfs and Wolf-Rayet stars, respectively. Fig. 10 gives some of the corresponding evolutionary tracks illustrating the evolutionary status of several objects discussed in this report. Main emphasis is given to AGB stars and their descendants. The evolution of AGB stars is mainly determined by (i) the recurrent thermal instabilities of the helium burning shell (*thermal pulses*), (ii) the convective envelope's penetration into the hydrogen burning shell for more massive objects (*hot bottom burning*), and (iii) strong and steeply increasing *mass losses* leading to the formation of circumstellar shells. One main effect of the He shell flashes is the mixing of interior carbon and s-process elements to the surface (third dredge up), i.e. the formation of carbon stars. A long-standing problem has been the so-called carbon-star mystery, i.e. the discrepancy that most of the carbon stars observed are found at low luminosities, indicating that they are of lower mass, whereas most AGB models predict the third dredge-up at much higher luminosities, i.e. large (core) masses. Another question is how to produce sufficient amounts of ^{13}C in the interior as the neutron source for the s-process nucleosynthesis.

The main weakness in confronting the observations with models is the only approximate description of stellar convection (and mass loss). It is often concluded that mixing may take place outside the formally convective boundaries. To overcome these problems, we have introduced overshooting based on the results of hydrodynamical simulations of convection by Freytag et al. (1996) to our treatment of convection. The parametrization of exponentially declining velocities of convective elements beyond the classical convective border then leads to some extra partial mixing. This method provided for AGB stars with rather *small* core masses of $\sim 0.6 M_\odot$ *both* a sufficient amount of dredge up *as well as* the production of ^{13}C as required by the observations. Furthermore, hot bottom burning can turn the carbon enriched envelopes of massive (and therefore luminous) models into nitrogen-rich ones. The question whether finally (more massive) carbon stars are formed is governed by the competition between dredge up and hot bottom burning, i.e. by the efficiencies of both processes which, in turn, depend on

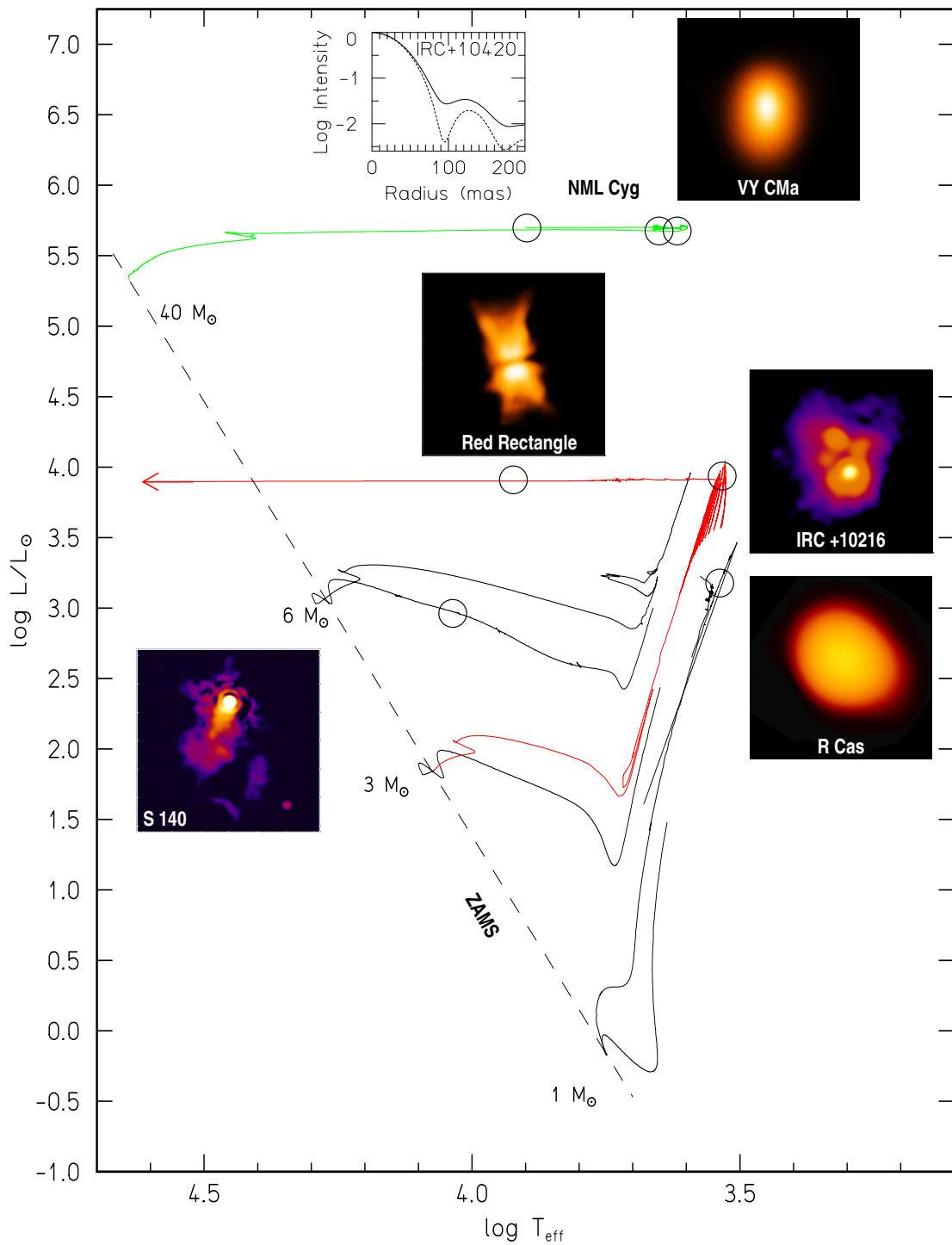


Figure 10: Illustration of the evolutionary status of several objects in early and late evolutionary stages (cf. Sec. 2) by comparison with evolutionary tracks calculated for initial masses of 1, 3, 6, and 40 M_{\odot} in the Hertzsprung-Russell diagram. The circles give the approximate loci of the objects, the dashed line delineates the zero-age main sequence. For clarity, the 1 M_{\odot} track is only shown up to the tip of the AGB, the 3 M_{\odot} track covers parts of the post-AGB phase as well, the 6 M_{\odot} sequence is only shown up to the Early-AGB, and the 40 M_{\odot} track ends before the Wolf-Rayet phase is reached. For $M \leq 6M_{\odot}$ the pre-main sequence evolution is shown as well.

the treatment of convection and mass loss. We investigate this important subject of chemical evolution by extensive evolutionary computations.

Regardless of their enrichment with heavier elements such as carbon or s-process elements, envelopes of AGB stars stay hydrogen rich. However, 20% of all post-AGB stars are found to be hydrogen deficient and the evolutionary history of these stars is not well understood. We calculated evolutionary post-AGB sequences, during which the stellar surface chemical composition changes from hydrogen-rich to strongly hydrogen-deficient as consequence of a very late thermal pulse, following the so-called *born-again scenario*. The internal structure and abundance changes during this pulse are computed with a numerical method which allows the physically consistent calculation of stellar layers where the thermonuclear and mixing time scales are comparable – a situation which occurs when the helium flash driven convection zone extends to the hydrogen-rich surface layers during the pulse peak. These models are the first to achieve general agreement with the surface abundance pattern observed in hydrogen-deficient post-AGB stars – e.g. the PG 1159 stars or the WR-type central stars of planetary nebulae –, strenghtening the born-again scenario with a physically consistent calculation and supporting the occurrence of convective overshooting in thermally pulsing AGB stars.

Currently, we are expanding our stellar evolution code to treat also effects of rotation on the structure and evolution of stars. For this purpose we have already included structural effects, angular momentum transport, and rotational mixing processes. We will focus on the evolution on the AGB and beyond since up to now it is only poorly known how rotation affects these important evolutionary stages in detail.

People involved: T. Blöcker, T. Driebe.

Collaborations: B. Freytag, H.-G. Ludwig (Univ. Kopenhagen); F. Herwig, N. Langer (Univ. Potsdam); D. Schönberner, M. Steffen (AIP, Potsdam); H. Holweger, W. Stolzmann (Univ. Kiel); R. Waters (Univ. Amsterdam)

3 The Seyfert galaxy NGC 1068

The different appearance of type 1 and 2 Seyfert galaxies is explained by the different orientation of a dusty gas torus (edge-on: Seyfert 2; face-on: Seyfert 1; unification scheme). The Seyfert 2 galaxy NGC 1068 is one of the nearest and brightest Seyfert galaxies (distance ~ 14 Mpc). Therefore, it is one of the best candidates for direct testing of the predictions of the unification scheme of AGN.

In 1996 we recorded first *K*-band speckle interferograms of NGC 1068 with the SAO 6 m telescope and resolved the core of NGC 1068 for the first time. A diffraction-limited elongated image with 76 mas resolution was reconstructed from the speckle interferograms using our bispectrum speckle interferometry method. The decreasing visibility function and the image have shown that the azimuthally averaged diameter of the resolved core is ~ 30 mas ~ 2 pc for an assumed Gaussian intensity distribution. In 1997 we continued our observations, confirmed the 1996 observations, and resolved additional structure.

Fig. 11 shows (left) the average of all obtained visibility functions of NGC 1068, (center) cuts through the visibility function along its major and minor axes, and (right) our 76 mas *K*-band image derived from all available data. The visibility function shows that the compact 30 mas component is elongated and has a size (FWHM Gaussian diameter) of $22 \text{ mas} \times 40 \text{ mas} \sim 1.6 \text{ pc} \times 3 \text{ pc}$. Our data allow us to put an upper limit to the height of a constant visibility

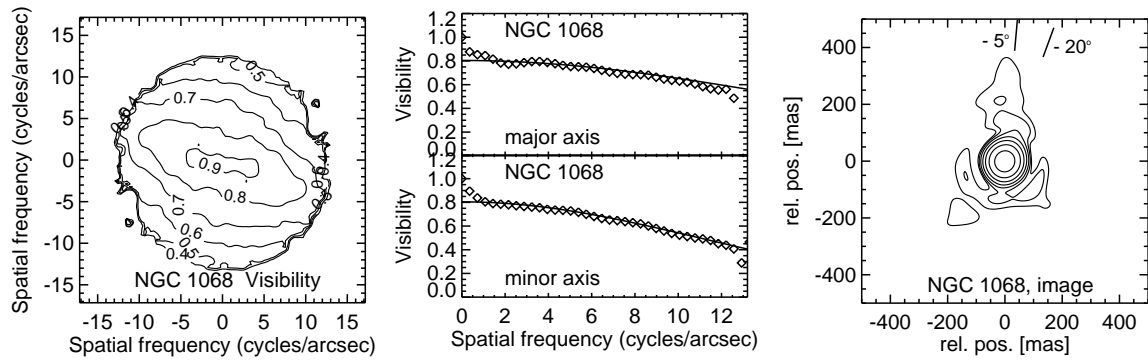


Figure 11: (left) Two-dimensional K -band visibility function of NGC 1068, (center) cuts through the visibility function, and (right) K -band bispectrum speckle interferometry image of NGC 1068; contour levels are at 1%, 2%, 4%, 8%, 16%, 32%, 64% of the peak intensity.

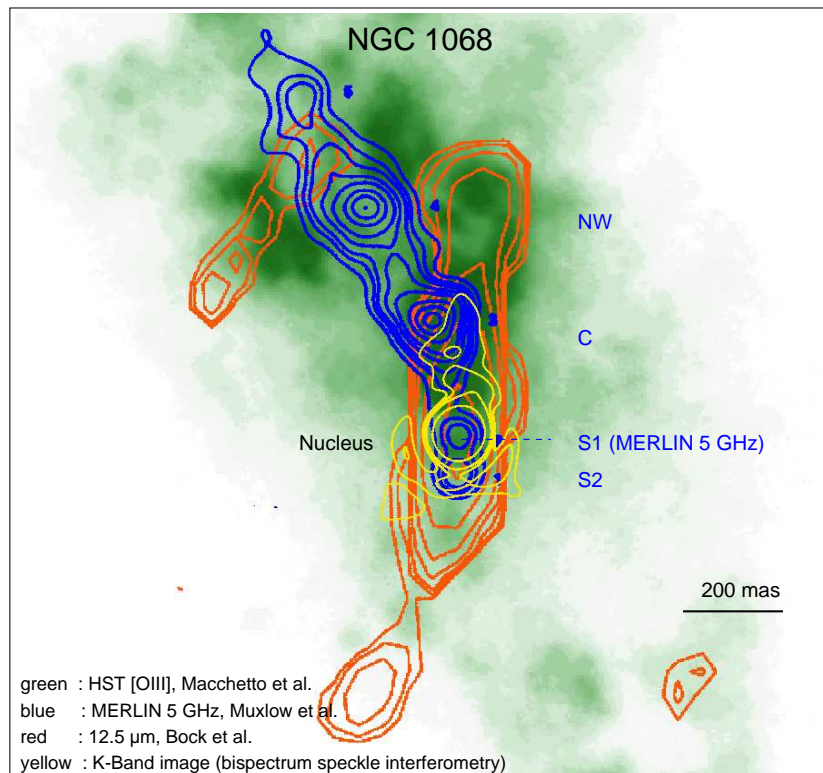


Figure 12: Comparison of our K -band reconstruction of NGC 1068 (yellow) with the [OIII] HST image (green), with the 5 GHz MERLIN image (blue) and with the $12.5 \mu\text{m}$ image (red). North is at the top, east to the left.

component due to an additional unresolved point source. The value of the visibility at the diffraction cut-off frequency shows that the height of such a constant component is smaller than 40% and, therefore, the flux of an unresolved component is less than 40% of the total flux in our field of view of $3''$. Furthermore, the visibility function shows a low-frequency peak which is caused by an extended component (northern extended component in Fig. 11,

right). Figure 11 (right) shows our reconstructed image. The position angles of the compact $22 \text{ mas} \times 40 \text{ mas}$ component and the extended northern component are $\sim -20^\circ$ and $\sim -5^\circ$, respectively.

Figure 12 shows a composite image consisting of the HST FOC [OIII] image, the MERLIN 5 GHz map (Muxlow et al. 1996), a $12.5 \mu\text{m}$ image (Bock et al. 1998) and our K -band reconstruction. The position of the nucleus is assumed to be at the intensity peak of the infrared images, at the apex of the optical conus and at radio component S1, the only radio component with a positive spectral index. The $12.5 \mu\text{m}$ emission seems to coincide with the wall of the optical conus near the nucleus. Our extended northern K -band component is also in alignment with this wall. Our compact K -band component with position angle of approximately -20° is neither aligned with one of the structures in the composite image nor with the VLBA torus image with position angle $\sim 106^\circ$ (Gallimore, Baum, O’Dea 1997).

Our interpretation of the resolved components can be summarized as follows. The compact $22 \text{ mas} \times 40 \text{ mas}$ component (position angle -20°) is probably caused by dust located in the region between broad-line region and narrow-line region above and below the torus. This dust emits thermal K -band light and scatters K -band light emerging at the inner edge of the torus and at the central continuum source. The unresolved point source is probably thermal radiation from the inner edge of the torus reaching us directly and possibly additional non-thermal direct light from the central continuum source. The extended northern component reaches out to a distance of $\sim 350 \text{ mas}$ or 20 pc , where dust is too cold to emit K -band light. We interpret the extended northern component as light scattered at electrons and dust forming the wall of the conus.

People involved: M. Wittkowski, K.-H. Hofmann, G. Weigelt.

Collaborations: Y. Balega (SAO); T. Beckert (Harvard); W. Duschl (Univ. Heidelberg)

4 Infrared long-baseline interferometry

In a few years infrared long-baseline interferometry will revolutionize infrared astronomy as radio interferometry revolutionized radioastronomy during the last decades. The VLT and the Keck interferometers will soon provide infrared images with the unprecedented resolution of $\sim 3 \text{ mas}$. Our main future aim is infrared interferometry with the LBT interferometer in Arizona and the VLT interferometer (VLTI) of ESO. We have started to develop instrumentation for the VLTI within the international VLTI AMBER Camera consortium, and have carried out observations with the IOTA and GI2T interferometers as discussed in detail below.

People involved: K.-H. Hofmann, D. Schertl, G. Weigelt.

Collaborations: J. Angel, J. Hill, P. Strittmatter (Steward Obs.); T. Herbst, H.-W. Rix (MPIfA); F. Malbet (Univ. Grenoble); D. Mourard, R. Petrov, P. Stee, F. Vakili (Univ. Nice); A. Richichi (Univ. Florence); M. Schöller (ESO)

4.1 Observations with the IOTA interferometer

Figure 13 shows one of several thousand recorded IOTA Michelson interferograms and the derived visibility measurements of five Mira stars. For the Mira stars X Oph, R Aql, V CrB, RU Her, and R Ser the uniform-disk diameters of 11.7 mas , 10.9 mas , 7.9 mas , 8.4 mas , and

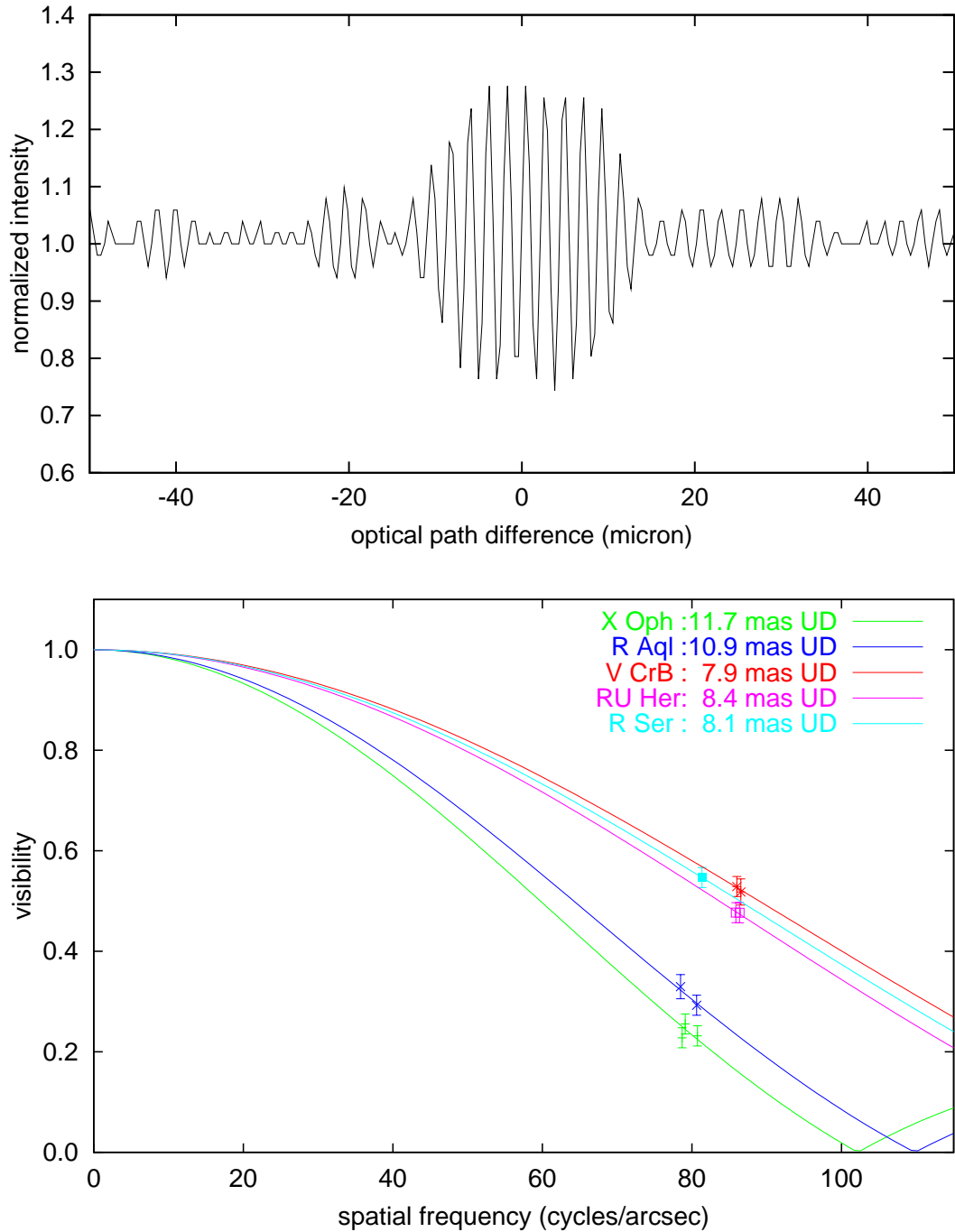


Figure 13: (top) IOTA interferogram and (bottom) visibility measurements of the five Mira stars X Oph, R Aql, V CrB, RU Her, and R Ser.

8.1 mas (± 0.3 mas) were derived, respectively. Simultaneous photometry by a collaborator allowed the determination of bolometric magnitudes and effective temperatures. Our future aims are studies of diameter variation with phase, asymmetries, wavelength dependence of the center-to-limb brightness variation, and comparisons with theoretical models (as discussed in section 2.1).

People involved: K.-H. Hofmann, D. Schertl, G. Weigelt, M. Wittkowski.

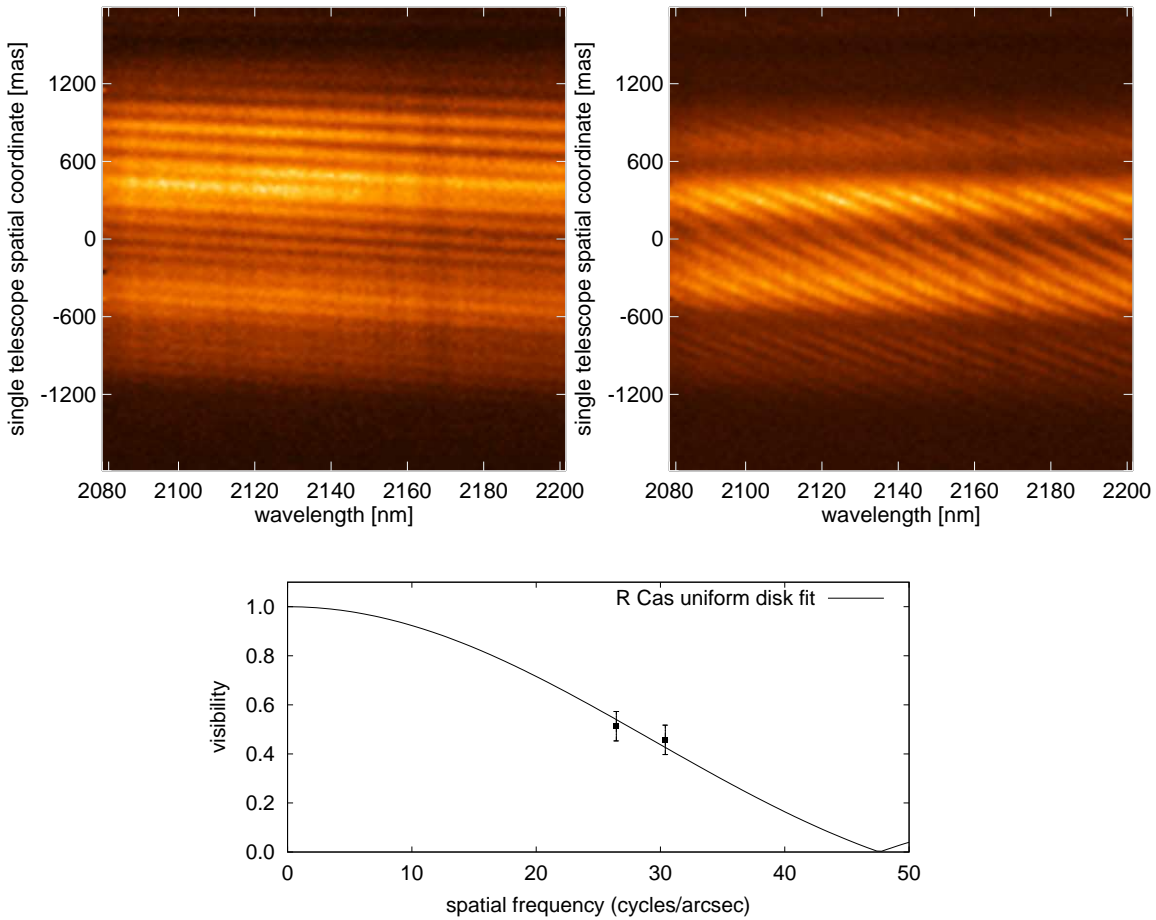


Figure 14: (top) GI2T interferograms recorded with our new infrared dispersed-fringe beam combiner (spectral range 2.08 to 2.20 μm , baseline 14 m) and (bottom) visibility measurements of R Cas (baselines 12 m and 14 m).

Collaborations: V. Coude du Foresto (Univ. Paris); M. Lacasse, W. Traub (CFA)

4.2 Infrared spectro-interferometry: first observations with the GI2T interferometer and our new dispersed-fringe beam combiner

The GI2T interferometer in France is an optical interferometer which consists of two 1.5 m telescopes with a maximum baseline of 50 m. For this interferometer we have built an interferometric beam combiner which is, for the first time, able to record spectrally dispersed Michelson interference fringes in the infrared. This type of beam combiner has two important advantages. First, it allows to simultaneously record Michelson interferograms in about 128 different spectral channels from 2.08 to 2.20 μm . The second advantage is that the tilt of the spectrally dispersed fringes is a measure of the instantaneous optical path difference (OPD). Figure 14 shows two of several thousand recorded interferograms of the Mira star R Cas. In the left interferogram the fringes are nearly parallel to the dispersion direction from 2.08 to 2.2 μm since the OPD error is nearly zero. In the right interferogram the fringes are tilted due to a small OPD error. The bottom panel shows our visibility observation of R Cas. From

the visibility curve the average uniform-disk diameter of R Cas was derived to be $25.1 \text{ mas} \pm 3.0 \text{ mas}$.

Our GI2T observations are the first NIR long-baseline interferometry observations with large (1.5 m) telescopes. The strongest current GI2T limitation is that the optical star tracker only allows observing objects down to $m_V = 7$. Therefore, we have started to design a new infrared system which consists of an infrared beam combiner, an infrared star tracker, and an infrared fringe tracker. The limiting K -magnitude of this system will be approximately $m_K = 10$. It will allow us to study many important evolved stars, a large number of young stellar objects in Taurus and Orion and, for the first time, several of the nearest Seyfert galaxies.

People involved: K.-H. Hofmann, D. Schertl, G. Weigelt.

Collaborations: D. Mourard, P. Stee, F. Vakili (Univ. Nice)

4.3 The VLTI AMBER instrument

Our most important future interferometry project is near-infrared interferometry with the ESO Very Large Telescope Interferometer (VLTI) and its AMBER beam combiner system. The AMBER instrument is a fiber optics beam combiner for measuring visibilities with very high precision (10^{-4}). The limiting magnitude is expected to be $K = 20$ if a bright reference star is available in the isoplanatic field and $K = 14$ otherwise. The main scientific objectives are investigations of young stellar objects, evolved stars, and AGN with high spatial resolution (3 mas for the wavelength $1.7 \mu\text{m}$ and baseline 120 m) and high spectral resolution (1000 to 10 000). AMBER is being built by an international consortium of institutes in France, Italy, and Germany. The Observatoire de la Côte d'Azur in Nice and the Laboratoire d'Astrophysique in Grenoble are responsible for the optics of the instrument, the instrument control, and data reduction software. The Osservatorio Astrofisico di Arcetri is building the spectrograph. Our MPIfR group is developing the detector, the real-time processing system, and data reduction software.

People involved: K.-H. Hofmann, T. Blöcker, D. Schertl, G. Weigelt.

Collaborations: F. Malbet (Univ. Grenoble); R. Petrov (Univ. Nice); A. Richichi (Univ. Florence); M. Schöller (ESO)

5 Origin of the highest energy cosmic rays and active galactic nuclei

Among the key results are (a) a limit of growth for black holes in the center of galaxies, (b) a model for the torus of dense gas in active galactic nuclei, and (c) a proposed correlation between ultra-high energy cosmic rays and compact radio quasars, which allows to go beyond the standard model in particle physics, to supersymmetry. In connection with our work on cosmic rays we also develop models for stellar and galactic winds.

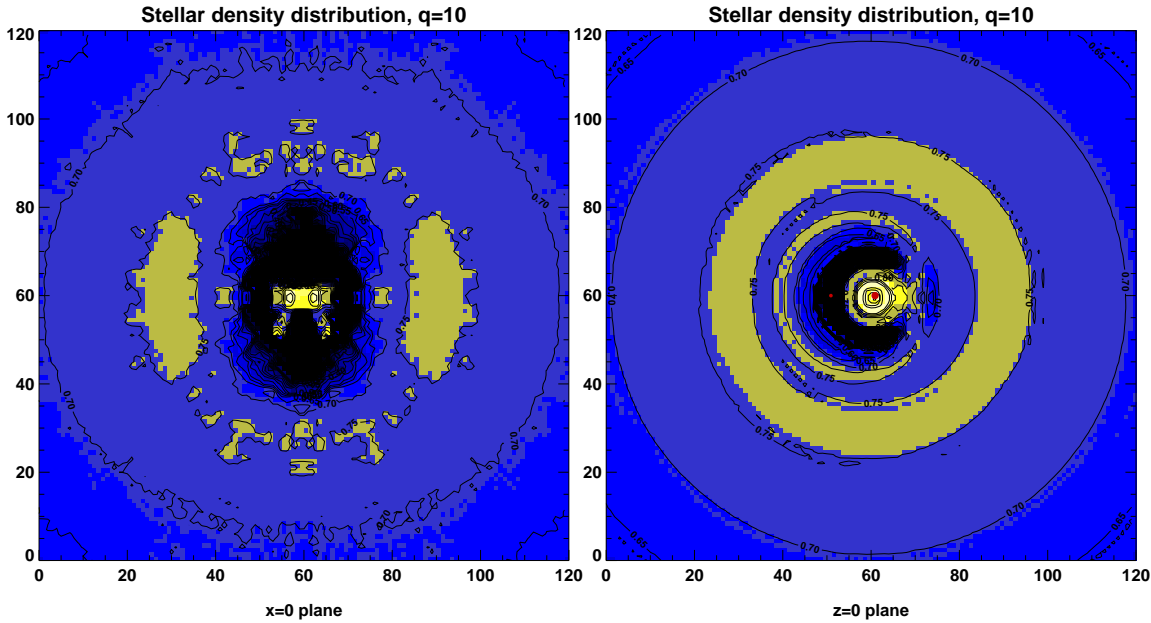


Figure 15: The stellar density enhancements around binary black holes in a cut perpendicular to the orbital plane (left), and in the orbital plane (right). The mass ratio of the two black holes is 10 in this example. The two black holes are shown as red dots.

5.1 Limits of Growth for Black Holes

Observations with the Hubble Space Telescope have demonstrated that most, if not all, galaxies have a central black hole of substantial mass. The mass of the black hole is proportional to the observed mass of stars in the spheroidal component of the host galaxy, or less. The present and past activity connected to the growth of such black holes have important consequences for the structure of galaxies and their evolution.

It has been possible to show that such a limiting proportionality arises naturally, if one considers a galaxy as a giant accretion disk. This concept had already been used successfully to understand the exponential disk distribution of stars in galaxies. The central black hole is fed from the inner boundary of an accretion disk that produces stars everywhere. A fairly high average viscosity is required in the inner region of a galaxy to allow accretion. There has to be strong turbulence, which explains the flow field also in our Galactic center region. This flow field shows strong evidence for overall accretion as shown in earlier work. Galaxies merge, and every merger heats the disk, turning the stellar disk into a component of the spheroidal stellar population. This consideration starts with stellar mass black holes. There is no free parameter in the system, and one naturally obtains a limiting ratio of a few hundred between the spheroidal stellar mass and the central black hole, as observed.

5.2 A model for the torus in AGN

In the context of the “Unified Scheme” of Active Galactic Nuclei there is always a torus of absorbing molecular material.

We have explored two lines of reasoning to explain this torus of absorbing material, one involving magnetic fields and cool but weakly ionized gas, and the other involving red giant stars and their wind turned tails. The far infrared emission of this torus has successfully been

modeled by many, including us. Using this radiation field, it has been possible to demonstrate that at photon energies beyond 1 TeV the emission must arise far from the central source, at a distance of order 0.1 to 1 parsec, despite the noted variability. Extreme variability at large distances from the central engine is also observable in the “Intraday variability”, observed at radio wavelengths for many flat spectrum radio source quasars; all of the GeV and TeV “blazars” are in this latter class. The torus can be modeled with magnetic support as the key ingredient, a model which may also work for similar structures around active stars.

We have been able to show that as one consequence of a merger between two galaxies, both of which possess a central black hole, the gradual approach of the two black holes produces a shell of stars around them. Stellar winds pushed out to form long tails from these stars can then absorb emission from the central engine, and so configure the torus. Thus, the torus is interpreted in such a concept as the sum of the long tails from the many red giant stars, that form part of the stellar population, that arranges itself in a torus like geometry as the result of the interactions with two black holes, circling each other. In Fig. 15 (right panel) we show an equatorial cut through the density distribution of stars, and in Fig. 15 (left panel) a vertical cut (perpendicular to the orbital plane of the two black holes). In both cases we used a mass ratio between the two black holes of 1:10.

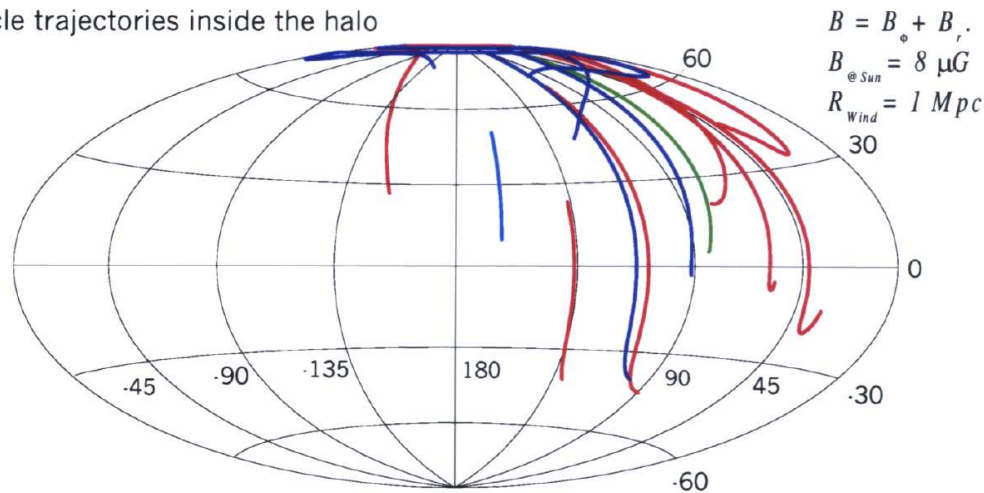
5.3 Cosmic Rays and Particle Physics

The origin of cosmic rays is still an open question, which is at the core of our work. We focus on the highest energies.

For those high energy cosmic ray particles, which are protons or heavier nuclei, one can follow the orbits backwards, through the local galactic halo. Modeling this halo as a wind, in a full but simple analogy with the solar wind or the wind of Wolf-Rayet stars, we find that almost all high energy events can be traced back to a direction consistent with the active galaxy M87 in the Virgo cluster. This orbit calculation does not involve scattering, but just bending. M87 had been argued some time ago to require protons up to 10^{21} eV to explain optical observations of an ubiquitous cutoff in the synchrotron emission at $3 \cdot 10^{14}$ Hz, seen all along its jet, as well as in many other sources of very different properties. This explains then both the higher particle energies observed (now 24 events claimed above 10^{20} eV, with new or newly analyzed events in 1999 from AGASA, HIREs, and Yakutsk), and the near isotropy found. In Fig. 16 we show the directions as traced on the sky, for the 14 events fully published. The very highest particle energies may require somewhat different physics, as described below.

Following earlier work by G.R. Farrar with the Fermi-Lab group that there may be a long-lived particle in supersymmetry, the S_0 , other avenues were explored to understand the origin of the highest energy cosmic ray particles. The S_0 is a combination of the u , d , s quarks with a gluino, has no charge, and a mass estimated to be near 2 GeV. In this version of supersymmetry the S_0 particle is sufficiently long-lived, and has zero interaction with the microwave background. This latter property is due to a threshold energy which is too high, so that the particle will interact with the far-infrared background, which we now know to be very low. Therefore the S_0 can traverse the universe from high redshifts. Following this line of reasoning it has been asked whether there might be any correlation between the arrival direction of the highest energy particles and distant radio quasars. Concentrating on the five best documented events with the highest energies, we indeed found a suggestion of such a correlation. Judging from a Monte-Carlo to simulate the error propagation in this analysis, it

Particle trajectories inside the halo



Galactic coordinates

Figure 16: All published ultra-high energy particle events above 10^{20} eV with their directions at Earth, and traced back in their direction to outside the Galactic halo. All orbits are consistent with an origin from the active galactic nucleus M87. A Parker-model is used for the magnetic field of the halo, a wind with total size 1 Mpc, an azimuthal magnetic field with $8 \mu\text{G}$ at the location of the Sun, and a much weaker radial field.

has been determined that the chance of a purely statistical coincidence in correlation between these events and distant quasars by fluke is only 1 in 200, and thus we conclude that the association is true. In addition, what gives considerable weight to the suggestion is that one uniquely identifies the one single class of quasars, which may comprise both a powerful accelerator and a beam dump; the CO(4-3) line has recently been used by others to show that some radio galaxies have indeed 10^{11} solar masses in gas around them, just the level of gas implicated in a beam-dump picture. Such sources are called “Giga-Hertz-peaked sources” or “Compact steep spectrum sources” in the language of radioastronomy. The source 3C147, well observed in Bonn, is one in our sample of identifications. Once we have been able to verify this hypothesis, it would give a very powerful hint to particle physics beyond the standard model, to a particular version of supersymmetry. If we succeed, we will be able to know where to start looking also for the lightest stable supersymmetric particle, which is widely expected to be the best candidate for cold dark matter.

People involved: P.L. Biermann, G. Bayer, A.C. Donea, F. Donea, T.A. Enßlin, L. Haroyan, C.-Y. Ma, S. Markoff, G. Pugliese, I. Roussev, H. Seemann, P. Simon, Y. Wang, Ch. Zier.

Collaborations: E.-J. Ahn (Seoul Nat. Univ.); J.A. Braatz (Harvard); T. Clarcke, P.P. Kronberg (Univ. Toronto); W. Duschl (Univ. Heidelberg); H. Falcke, C. Henkel (MPIfR); G. Farrar (New York Univ.); A. Fridman, M.M. Romanova (Acad. of Science, Moscow); T. Stanev (Bartol Res. Inst., Newark, DE); M. Harwit (Washington, DC and Cornell Univ.); H. Kang (Pusan Nat. Univ.); N. Kassim, R. Perley (VLA, Socorro); U. Klein, S. Kohle (Univ. Bonn); Gopal Krishna (Tata Inst., Pune); M. Lemoine, G. Sigl (CNRS, Paris); R. Lieu (Univ. Alabama); R. Lovelace (Cornell Univ.); K. Mannheim (Univ. Göttingen); G. Medina-Tanco (Univ. Sao Paolo); H. Meyer, B. Wiebel-Sooth (Univ. Wuppertal); B. Nath (Raman Res. Inst., Bangalore); L. Ozeroy (George Mason Univ.); R.J. Protheroe (Univ. Adelaide); J. Rachen (Univ. Utrecht); W. Rhode (Univ. Cal. Berkeley); A.S. Wilson (Univ. Maryland); D. Ryu (Daejeon Nat. Univ.); X.-P. Wu (Acad. of Science, Beijing).